Energy Materials

Article

Epitaxial growth of aligned MoS₂ via One-step CVD method for realizing the ultrasonic field-driven direct current nanogenerators

Jing Li[1,2], Jiangtao Guo[2], Yong Zhang[3], Ang Zhang[1,2], Wen Yang[2,*], Xiaobo Feng[2], Yunbo Zhang[2], Peizhi Yang[1,2,*]

[1]Southwest United Graduate School, Kunming 650092, Yunnan, China.
[2]Laboratory of Advanced Technique & Preparation for Renewable Energy Materials, Ministry of Education, Yunnan Normal University, Kunming 650500, Yunnan, China.
[3]Department of Electrical and Computer Engineering and Center for Optoelectronics, University of North Carolina at Charlotte, Charlotte, NC 28223, USA.

*Correspondence to: Prof. Peizhi Yang, Laboratory of Advanced Technique & Preparation for Renewable Energy Materials, Ministry of Education, Yunnan Normal University, Kunming 650500, Yunnan, China; Southwest United Graduate School, No. 298, Yieryi Street, Kunming 650092, Yunnan, China. E-mail: pzhyang@hotmail.com; Wen Yang, Laboratory of Advanced Technique & Preparation for Renewable Energy Materials, Ministry of Education, Yunnan Normal University, Kunming 650500, Yunnan, China. E-mail: wengyang1972@hotmail.com

Abstract

Molybdenum disulfide (MoS₂) is widely used in energy harvesting devices due to its high carrier mobility and semiconductor properties. However, the preparation of high-quality MoS₂ still faces significant challenges. In this work, we present a one-step chemical vapor deposition method for the preparation of large-size MoS₂ nanosheets with an orientation rate of over 70%. The one-step preparation method is more cost-effective and time-efficient compared to conventional techniques. The aligned MoS₂ nanosheets demonstrate a significant capacity for charge transfer in triboelectric devices. Herein, we propose a concept of MoS₂ as the charge transport layer for nanogenerator arrays for hybrid energy harvesting and high-performance direct output. Furthermore, the current density of the device exceeds 10 A/m² under ultrasonic excitation. Consequently, this finding is anticipated to offer new insights into applications such as mechanical energy conversion and MoS₂ charge transport.

Keywords: MoS₂, large size, one-step CVD method, MoS₂-based TENG

INTRODUCTION

As the miniaturization of silicon-based devices approaches the limits of their physical performance, there is an urgent need to develop novel materials to overcome the material limitations[1,2]. Transition-metal dichalcogenides (TMDs) have attracted considerable attention due to their exceptional physicochemical properties, including high carrier mobility and high current switching ratio. Molybdenum disulfide (MoS_2), as a representative of transition metal sulfides, exhibits a tunable bandgap. It undergoes a transition from an indirect bandgap to a direct bandgap when the material is reduced from bulk to a monolayer[3-5]. MoS_2 is widely used in various fields, including photovoltaic devices, logic devices, flexible devices, and photocatalytic hydrogen precipitation[6-9]. Compared with other TMDs, MoS_2 also exhibits superior characteristics in the field of charge transport and energy collection. MoS_2 possesses the capacity to enhance charge transport by controlling the number of layers[10] and reducing the number of grain boundaries and defects [11]. These characteristics make MoS_2 an ideal material for energy harvesting devices, supercapacitors and sensors[12-14].

A triboelectric nanogenerator (TENG) is an energy harvesting device based on contact charging and electrostatic induction coupling[15,16]. TENG is continuously innovated in combination with liquid metals, solar cells, and 2D materials[17-19]. Aji *et al.* and Kumar *et al.* improved the voltage and energy harvesting performance of TENG through the application of MoS_2 film[20,21]. Wang *et al.* used water and monolayer MoS_2 as friction layers to obtain high open circuit voltage and transfer charge[22]. However, this energy harvesting method still has shortcomings. Due to the presence of numerous grain boundaries and defects in MoS_2 film, significant losses may occur during the charge transfer process[23,24]. Therefore, the preparation of MoS_2 films with fewer grain boundaries and defects is a key current research interest.

MoS_2 films with reduced grain boundaries and defects are prepared through two strategies: (1) grain boundaries and defects can be avoided by growing only one grain on the substrate and continuously expanding the grain size; (2) controlling grain orientation can inhibit the formation of grain boundaries[25]. The chemical vapor deposition (CVD) method is widely employed to control grain orientation due to its capability to accurately regulate growth time, growth temperature and carrier gas flow rate[26-28]. Aljarb *et al.* obtained regularly oriented MoS_2 grains on sapphire by CVD method[29]. This results in smaller grain sizes and they were prone to spontaneous rotation to the energetically favorable position. It is determined by the lattice structure of the substrate, leading to preferred orientation and alignment of MoS_2. Density functional theory simulations demonstrate that MoS_2 deposited on sapphire has two preferred orientations[30]. Regrettably, the grain size of MoS_2 grown in this way was limited and the orientation rate is uncontrollable. Therefore, it is necessary to explore a method that can control the growth of aligned MoS_2. Subsequently, Park *et al.* employed $MoOCl_4$ and H_2S as precursors and annealed the sapphire at 1,000 °C for 6 h to facilitate the growth of MoS_2 in two aligned orientations, which suggests that the formation of etched surface on the sapphire was a prerequisite for obtaining single orientation of MoS_2[31]. Liu *et al.* achieved the successful growth of 99% oriented bilayer MoS_2 by annealing c-plane sapphire with mis-cut of 1° towards the a-axis for four hours in air[32]. These methods can obtain MoS_2 films with good morphology and high orientation rate. However, these preparation methods typically require a long annealing period and the introduction of hydrogen or oxygen to etch the substrate surface, resulting in a long growth time and small grain sizes of the film[33-35].

In this study, we propose a CVD one-step method for the preparation of aligned MoS_2. In Supplementary Table 1, we compared the parameters of the one-step method with those of other CVD methods for preparing molybdenum disulfide. This method significantly shortens the preparation time and reduces the raw material cost. MoS_2 was used as a charge-transporting layer to investigate the effect of

aligned MoS_2 on the electrical properties of the TENG. In Supplementary Table 2, we compared the device with some TENG devices. The MoS_2-TENG device prepared by the one-step method has a strong charge transfer capability under the action of ultrasonic waves. This work provides a pathway for the synthesis of aligned MoS_2 and also explores the potential of the oriented MoS_2 in the TENG field.

## EXPERIMENTAL

Synthesis of aligned MoS_2

In this study, the CVD method is employed to prepare aligned MoS_2 nanosheets. Prior to the growth of aligned MoS_2, S (99.5%, 35 mg) and MoO_3 (99.95%, 0.5 mg) powder, used as precursors, were placed in two quartz boats (1.5 cm × 10 cm), respectively. The sulfur powder was placed in the first temperature zone and the MoO_3 was placed in the second temperature zone, with the two zones 15 cm apart. To fit the symmetry of MoS_2, we chose c-plane sapphire as the growth substrate. c-plane sapphire has a six-fold symmetry while MoS_2 has only two low-energy orientations on c-plane sapphire. Additionally, the substrate was miscut by 1° toward the crystal <11-20> axis, as illustrated in Figure 1A, with the objective of further reducing the symmetry of the substrate. As shown in Supplementary Figure 1A-D, the MoS_2 grown on the sapphire substrate without miscut exhibits a large area of stacking, resulting in an indistinct orientation. Sapphire with a miscut angle of 2° has a relatively small growth size and poor morphology. The grains of sapphire with a miscut angle of 4° are severely damaged. We compared the sizes of MoS_2 grown at different temperatures, as shown in Supplementary Figure 1E-G. With the increase of temperature, the grain size of MoS_2 increases. Based on this, the curve of the growth of MoS_2 grain size with temperature was plotted [Supplementary Figure 1H]. Therefore, considering factors such as orientation rate and grain size, we choose substrate miscut angle of 1° and grain growth temperature of 1,000 °C. As illustrated in Figure 1B and C, the sulfur powder, MoO_3, and substrate were placed in three distinct temperature zones, because the annealing temperature of sapphire of 1,000 °C exceeds the evaporation temperature of MoO_3. The third temperature zone was initially elevated to 1,000 °C and maintained for 70 min. The first and second temperature zones were then increased to 100 and 500 °C, respectively, ensuring that the sulfur powder and MoO_3 did not evaporate and the temperature rose rapidly to the desired deposition temperature, following annealing of the sapphire substrate. The first temperature zone remained for 140 min and then rose to 86 °C within 20 min. The second temperature zone remained for 83 min and then rose to 870 °C within 37 min. In this way, when the annealing of the third temperature zone is completed, the first and second temperature zones can reach the deposition temperature simultaneously. After the sapphire substrate annealing was completed, without the cooling substrate, the temperature of the first temperature zone and the second temperature zone were directly increased to 286 and 870 °C, respectively. After the deposition was completed, the aligned MoS_2 was obtained.

Fabrication of MoS_2-based TENG

The synthesized MoS_2/sapphire is fixed on an acrylic plate (20 mm × 30 mm × 0.1 mm). After an Ag electrode has been plated on the substrate by a coating machine, the liquid metal is spin-coated onto the Ag tape and affixed on top of the plated Ag electrode. Subsequently expanded polytetrafluoroethylene (E-PTFE) is covered over the Ag electrodes and seamlessly connected to the substrate, connecting the two ends of the Ag electrodes to form a closed circuit.

Characterizations and measurements

Optical microscopy (OM, Nikon LV100), scanning electron microscopy (SEM, ZEISS Gemini Sigma 300), and atomic force microscopy (AFM, Bruker Dimension Icon) probes adopt the contact mode, and the test area is the boundary between MoS_2 grains and the substrate. The height difference between MoS_2 and the substrate was measured by NanoScope Analysis software. The MoS_2 grains were tested by X-ray photoelectron spectroscopy analysis (XPS, Thermo Fisher Scientific K-Alpha), and the C 1s peak (284.8 eV)
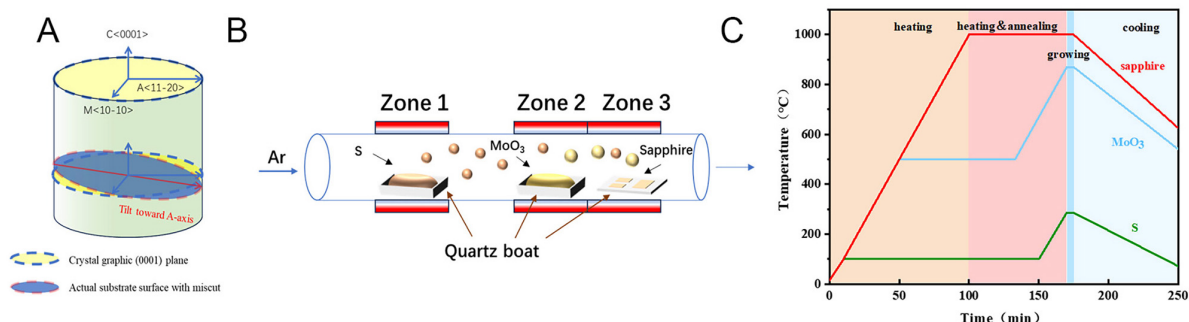
Figure 1. (A) Schematic illustration of the miscut of the sapphire wafer from an ingot. (B) Schematic diagram of the CVD system for MoS$_2$ synthesis. (C) Schematic diagrams of the growth temperature ramps.

was employed as a reference for calibration. Raman spectroscopy (HORIBA JY LabRAM HR Evolution with 532 nm laser) was used to characterize the synthesized MoS$_2$. Polarized second-harmonic generation (SHG) microscopy measurements were performed in a homemade system. A femtosecond laser with 780 nm central wavelength (~100 fs, 100 MHz, generated by MenloSystems) and power of 1.8 mW was used to excite the sample. The laser beam passed through a linear polarizer and was tightly focused to ~1 μm spot diameter by a 100× objective (NA = 0.9, Nikon). The MoS$_2$ samples were attached to a piezoelectric stage to realize sub-micrometer scanning. Analog-to-digital conversion (ADC) collection system (Keithley 6514) was used to measure the charge, voltage and current.

RESULTS AND DISCUSSION
Growth mechanism of aligned MoS$_2$
When the substrate symmetry is a subset of the 2D material, the 2D material has fewer low-energy orientations on the substrate[36]. As shown in Figure 2A, MoS$_2$ with threefold symmetry has two low-energy orientations on a two- or six-fold symmetry substrate, and four low-energy orientations on a four-fold symmetry substrate. Two strategies have been identified for the growth of aligned MoS$_2$: (1) Direct growth is achieved by exploiting the symmetry of MoS$_2$ and the substrate. When the symmetry of the substrate lattice is matched with that of MoS$_2$, MoS$_2$ is able to achieve less orientation variant growth. This strategy typically necessitates the assistance of hydrogen or oxygen during the growth process[37] and it is incompatible with the single orientation growth of MoS$_2$; (2) Substrate pretreatment. Steps are formed by annealing, lithography, and etching of the substrate[38]. The MoS$_2$ edges have higher binding energy at the edges of the steps, thus realizing the aligned growth.

In this process, the pretreatment of the substrate is employed to create steps on the sapphire through annealing. As shown in Figure 2B, the initial sapphire surface is disordered, and parallel steps appear on the sapphire surface after annealing. These steps promote MoS$_2$ aligned growth. Figure 3A and B shows the AFM image of sapphire without and with annealing treatment. Figure 3C corresponds to the height profile of the red line in Figure 3B and D shows the OM image of the CVD deposited aligned MoS$_2$. The results indicate that the height of the steps is approximately 200 pm. Ultimately, the MoS$_2$ grains exhibit alignment growth.

One-step preparation of aligned MoS$_2$
The conventional methods for the preparation of aligned MoS$_2$ typically necessitate prolonged annealing in air or oxygen atmosphere[39,40]. The substrate must await the cooling of the temperature zone after the annealing period of one to four hours before commencing the substrate next growth process, and the total duration of the annealing step exceeds 8 h. This approach is exceedingly time-consuming and energy-consuming. Meanwhile, it significantly increases the preparation cost.
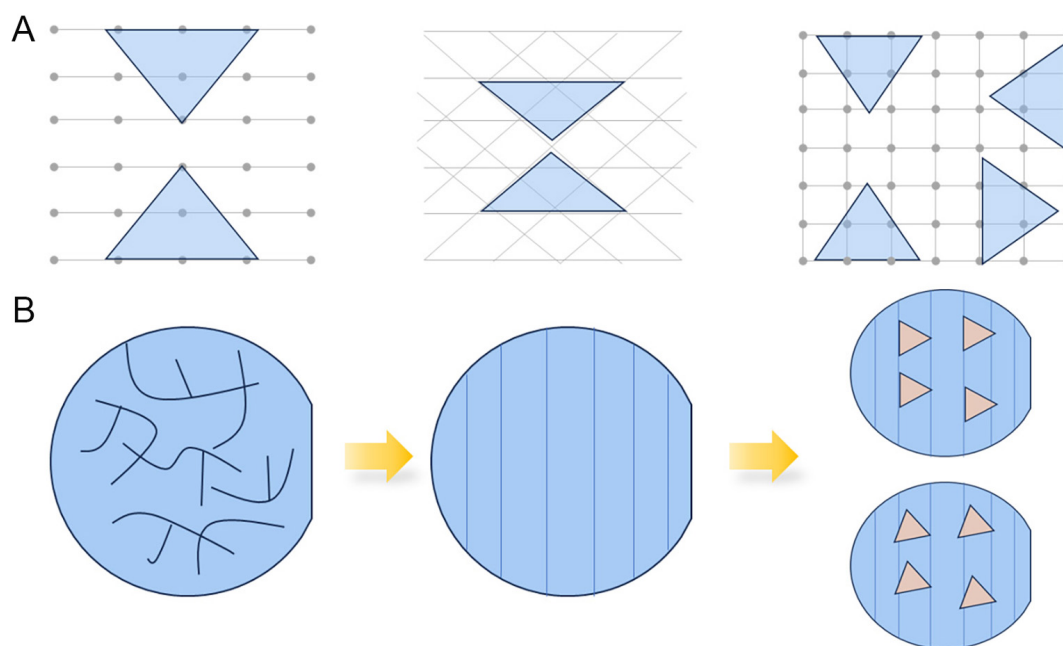
Figure 2. (A) Schematic illustration of a threefold symmetric 2D material on a two-, six-, and four-fold symmetric substrate, respectively. (B) Schematic illustration of the sapphire parallel steps formation and MoS$_2$ growth process.
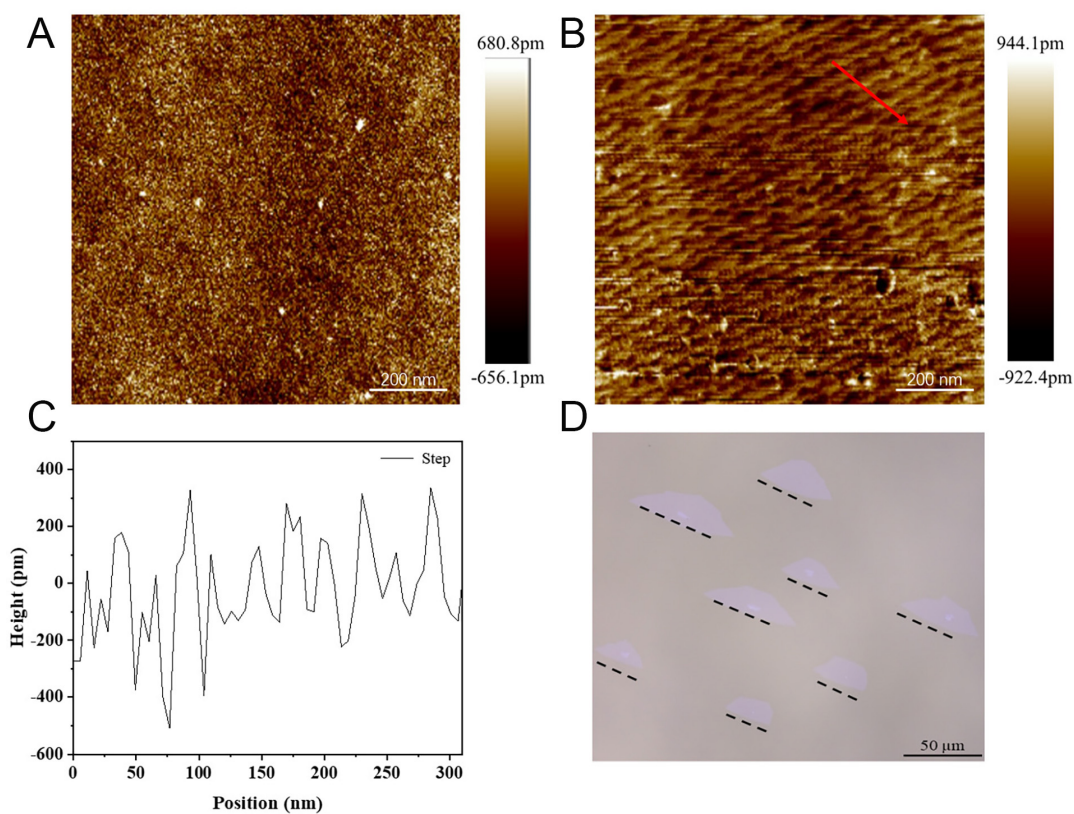
Figure 3. (A) AFM image of sapphire before annealing. (B) AFM image of sapphire after annealing. The height profile (C) is along the red lines in (B). (D) OM image of the CVD deposited aligned MoS$_2$.

Here, we observe that the short annealing time is sufficient to form steps on the substrate. When the steps are formed, the initial nucleated MoS_2 grains tend to preferentially deposit at the edge of the step. The precursor is directly transported from the low-temperature zone of the CVD to the third temperature zone, where it can be directly deposited to form aligned MoS_2 without cooling in the annealing temperature zone. This method simplifies the preparation steps of MoS_2, thereby reducing the preparation time and cost. As shown in Figure 4, we compare the samples produced by no miscut sapphire [Figure 4A], unannealed sapphire [Figure 4B], and annealed sapphire at 850 °C [Figure 4C] with the samples prepared by the one-step method [Figure 4D]. Samples without miscut sapphire have inferior morphology and are difficult to discriminate between the orientations. In addition, the MoS_2 grown from without miscut sapphire is prone to stacking in banded patterns. Samples of unannealed sapphire exhibit random orientations due to the absence of step formation. Because the growth temperature is 1,000 °C, its grain size reaches 100 μm. The smaller grain size of the 850 °C anneal compared to the 1,000 °C anneal is due to the fact that the high temperature of 1,000 °C makes the precursor gases more active and more evenly distributed on the substrate. Meanwhile, at 850 °C, no steps can be formed on the substrate, so the grains show random orientation.

In particular, 3 mg of molybdenum oxide is required for the sample at 850 °C, and only 0.5 mg is required for annealing at 1,000 °C. This is due to the fact that the temperature of the third zone is 1,000 °C and the temperature of the second zone is 850 °C. According to the $P\ V = n\ k\ T$ equation, there is a pressure difference between the third zone and the second zone[22,41], and the precursor gases tend to diffuse into the second zone and remain in the tube furnace for a longer period of time. Therefore, this method simplifies the preparation steps of MoS_2, reduces the preparation time and raw material costs, and is conducive to grain size increase and uniformity.

Characterization of aligned MoS_2

Figure 5A and B depicts the OM and SEM images of the prepared aligned MoS_2. From Figure 5A and B, it can be seen that the MoS_2 grains grow in the same direction, and the grain sizes range from 80 to 200 μm. The majority of MoS_2 grains exhibit a trapezoidal morphology, which is attributed to the high growth temperature. The insulation of the sapphire substrate impairs the clarity of the SEM image, preventing the determination of whether secondary growth occurs on the grain surface. It is evident that the MoS_2 has larger grain sizes and exhibits directional growth.

The photoluminescence (PL) spectra of the aligned MoS_2 and randomly oriented MoS_2 were obtained, as illustrated in Figure 5C. The aligned MoS_2 exhibited a notable quenching in PL intensity compared to the randomly oriented MoS_2, which was due to the strong coupling of the aligned MoS_2 with the substrate. To further investigate the strong coupling between aligned MoS_2 and the substrate, Raman spectroscopy tests were performed on aligned MoS_2 and randomly oriented MoS_2. As illustrated in Figure 5D, the rightmost peak is the sapphire substrate characteristic peak. We use the sapphire characteristic peak as a benchmark to compare the E_{2g} peak positions of the two MoS_2 samples. The E_{2g} peak position of randomly oriented MoS_2 is located at 385.1 cm^{-1}, while the E_{2g} peak position of aligned MoS_2 is noted at 381.6 cm^{-1}. The E_{2g} peak of aligned MoS_2 shows a red shift, demonstrating strong coupling between aligned MoS_2 and the substrate with tensile strain[42,43]. Annealing appears to have enhanced the epilayer-substrate bonding. In order to initially characterize the thickness of aligned MoS_2, the frequency difference between the peak positions of aligned MoS_2 E_{2g} and A_{1g} was calculated to be 22 cm^{-1}, which suggests MoS_2 to be around one monolayer thick[44,45].
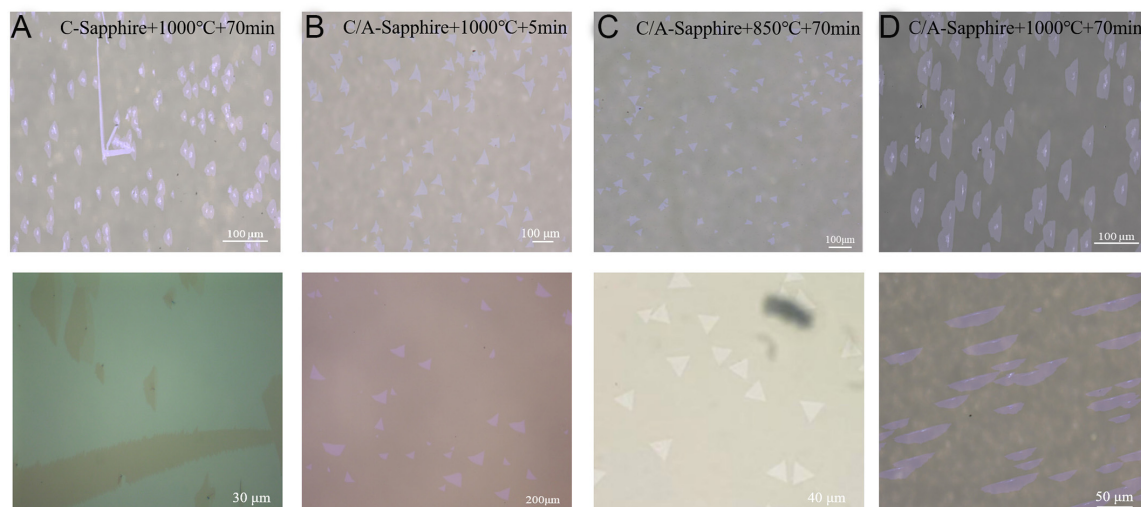
Figure 4. OM image of MoS$_2$ growing under different parameters.
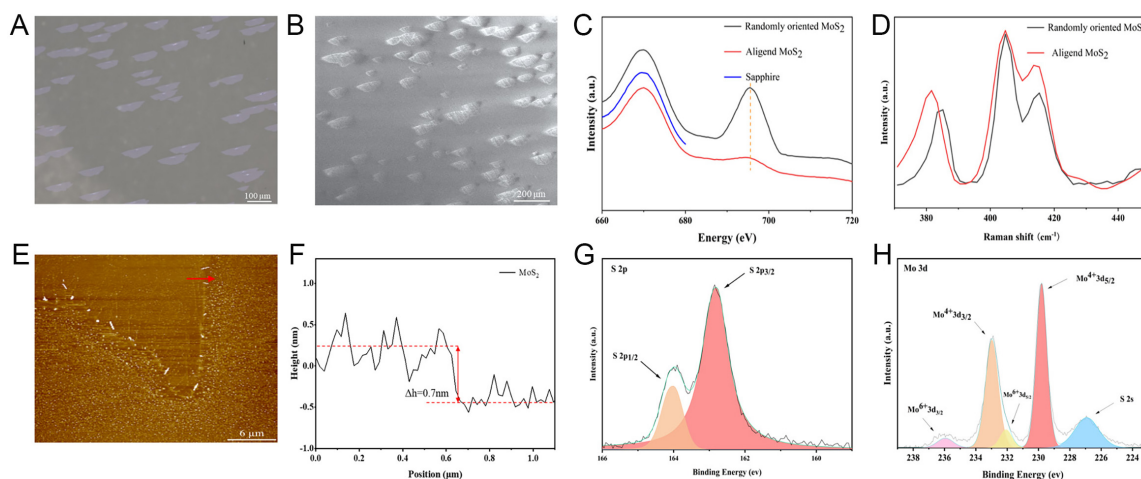
Figure 5. (A) OM image of the CVD deposited aligned MoS$_2$. (B) SEM image of the CVD deposited aligned MoS$_2$. (C) PL spectra of aligned MoS$_2$ (red line) and randomly oriented MoS$_2$ (black line). (D) Raman spectra of aligned MoS$_2$ (red line) and randomly oriented MoS$_2$ (black line). (E) AFM image of the MoS$_2$ flake. The height profile (F) is along the red lines in (E). XPS spectra of (G) S 2p and (H) Mo 3d.

The thickness of the aligned MoS$_2$ was accurately characterized by AFM, as illustrated in Figure 5E. Figure 5F depicts the height profile corresponding to the red line in Figure 5E. The aligned MoS$_2$ exhibits a thickness of approximately 0.7 nm, which is consistent with that of monolayer MoS$_2$ (0.65 nm).

To analyze the binding energy of the Mo and S atoms in the aligned MoS$_2$, XPS was performed. The C 1s peak (284.8 eV) was employed as a reference for calibration. The S 2p spectrum [Figure 5G] exhibits two characteristic peaks at 162.8 and 164 eV, which correspond to the S 2p$_{1/2}$ and S 2p$_{3/2}$ orbitals, respectively. The Mo 3d spectrum [Figure 5H] exhibits characteristic peaks at 236.1, 233.1, 232.1, 230, and 227.2 eV, which correspond to the Mo^{6+} 3d$_{3/2}$, Mo^{4+} 3d$_{3/2}$, Mo^{6+} 3d$_{5/2}$, Mo^{4+} 3d$_{5/2}$ and S 2s orbitals, respectively. The characteristic peaks are consistent with previous reports[46-48], indicating that the prepared sample has a relatively pure MoS$_2$ phase.

To ascertain the growth orientation degree of the MoS_2 grains, we selected six different sites [Figure 6A] on the same substrate for observation and analysis. Figure 6B-G depicts the OM images of the six locations. From Figure 4, it can be seen that most of the grain sizes are over 100 μm. The orientation of 233 grains on the substrate was counted using the image j software with the horizontal orientation as a reference. The schematic diagram is shown in the upper right corner of Figure 6H. As shown in Figure 6H, the grain orientation is mainly distributed in the range of 11°-16°, and 73.8% grains are distributed in the range of 12°-15°. This proves that the orientation rate of our prepared samples exceeds 70%.

To explore their lattice orientations and grain boundaries at merging, Polarized SHG characterizations were performed. Figure 7A shows the OM image of MoS_2 grains combined. Figure 7B demonstrates the SHG mapping image of the red region in Figure 7A. There is no decrease in intensity in the merged grains, indicating that no grain boundaries exist[38]. Figure 7C-F presents the five polarization resolved SHG patterns across a 1 cm^2 sample area. The nearly overlapped SHG six-petal patterns confirm the coherent lattice orientation and uniformity of the as-grown MoS_2 nanosheet[33].

Electrical performance testing of MoS_2-based TENG

The charge transfer characteristics at the interface between MoS_2 and E-PTFE were studied using TENG as a charge transfer probe and ultrasound as an energy source. The Ag electrode was evaporated on MoS_2 using the coater and mask, as illustrated in Figure 8A. Fix the sapphire after evaporating the electrode onto an acrylic plate (The MoS_2-based TENG photo is shown in Supplementary Figure 2). Due to the inability to directly connect the vaporized silver electrode to the alligator clips, the subsequent step involves spin-coating liquid metal onto silver tape. Attach the silver tape to the E-PTFE surface according to the width of the evaporated electrode and affix it on top of the vaporized Ag electrode. The particle size of the vaporized Ag electrode is small, and the direct adhesion of the Ag tape is not able to maintain the conduction. Spin-coating the liquid metal can improve the conduction ability of the Ag tape with the vaporized Ag electrode. In conclusion, the device is composed of MoS_2 on the bottom, vaporized Ag electrode, liquid metallic Ag tape, and E-PTFE on the top surface [Figure 8B].

In order to gain a deeper understanding of the operation principle of MoS_2-based TENG devices, the fundamental principle of charge generation and transfer between the MoS_2-PTFE layers during the operation of the ultrasonic generator is studied. As illustrated in Figure 8C, E-PTFE is electronegative. When MoS_2 and E-PTFE come into contact with each other, the electric-double layer is formed at the interface between the MoS_2 and E-PTFE. This is in equilibrium and there is no charge movement[17]. When ultrasonic waves are applied to the device surface, more negative charges accumulate on the E-PTFE surface and more holes appear on the corresponding MoS_2 surface. In order to establish electrostatic equilibrium, the electrons on the MoS_2 surface move in a directional manner to fill the holes, which are ultimately collected by the TENG probes.

The voltage, current, and charge generated by the MoS_2-based TENG under ultrasonic waves are studied. As illustrated in Figure 9A-C, when the ultrasonic generator is turned on and off, it is possible to observe the rise and fall of the voltage, current, and charge generated between the Ag electrodes at both ends. After the ultrasonic generator is stopped, both voltage and current cease to exist, and the accumulated charge is diminished. It is noteworthy that the MoS_2-based TENG can generate a voltage exceeding 120 V, a current of 1 mA, and accumulate a charge of 1,200 nC within a brief interval. From the area of the device (1 cm^2), a current density of 10 A/m^2 is obtained, indicating that the aligned MoS_2 has excellent charge transport performance.
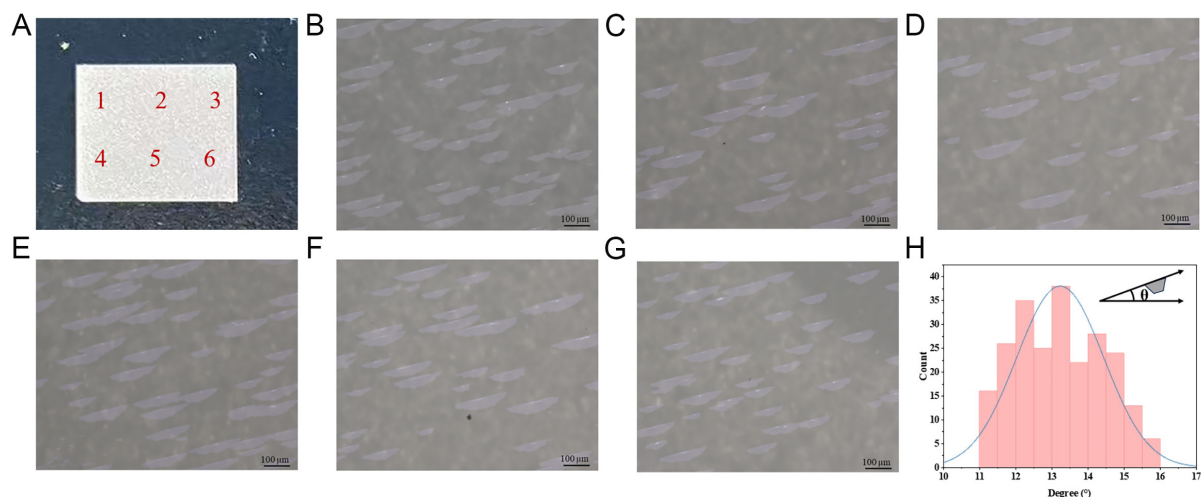
Figure 6. OM images for six positions on the sapphire, (B-G) correspond to 1-6 in (A). (H) Statistical distribution of MoS$_2$ domains.
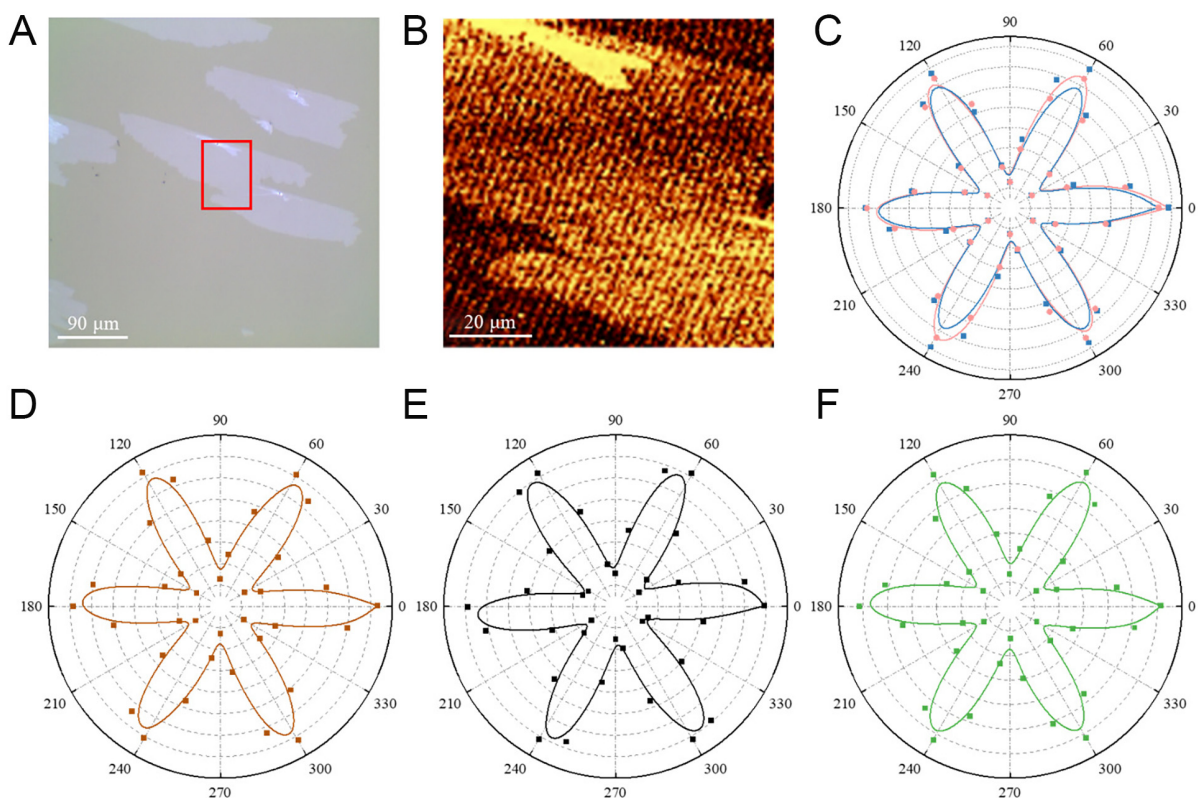

Figure 7. (A) OM image of two merging MoS$_2$ domains. (B) SHG mapping of two merging MoS$_2$ domains in the red region in (A). (C-F) Polar plot (°) of the SHG intensity of five MoS$_2$ grains on the same substrate.

In order to investigate the effect of ultrasonic power on charge transfer, we measured the voltage, current and charge of the electrodes at both ends of the device for 5 s at 10-50 W power, respectively. As illustrated in Figure 10A-C, the current voltage magnitude and charge accumulation rate of the MoS$_2$-based TENG increase with the increase of the ultrasonic power. Ultrasonic waves accelerate the charge movement in the
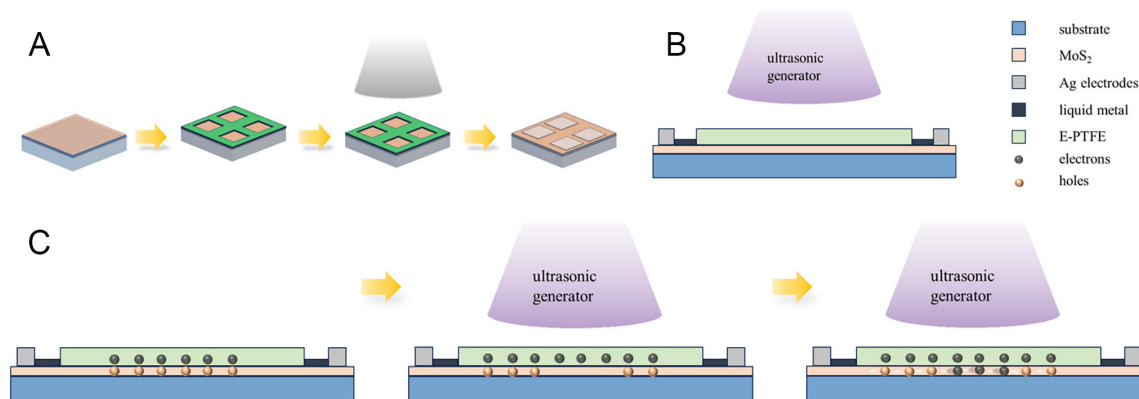
Figure 8. (A) Schematic diagram of silver electrode vaporization. (B) Schematic structure of MoS$_2$-based TENG. (C) Working mechanism of the MoS$_2$-based TENG.
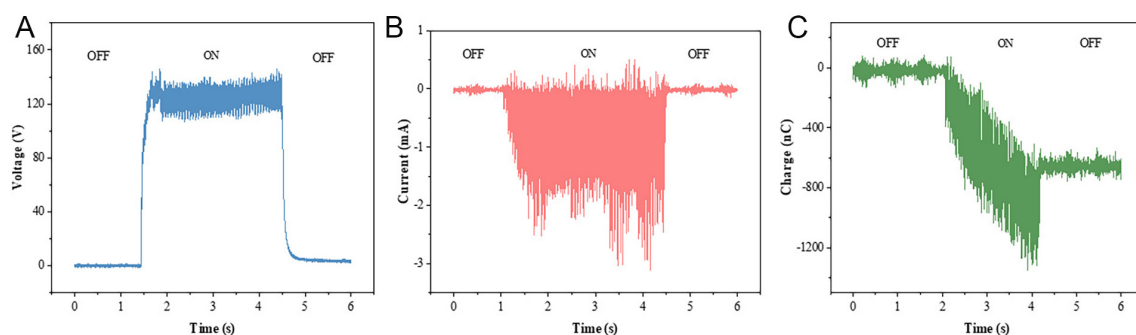
Figure 9. MoS$_2$-based TENG voltage (A), current (B), and charge (C) in the ultrasonic on-off state.
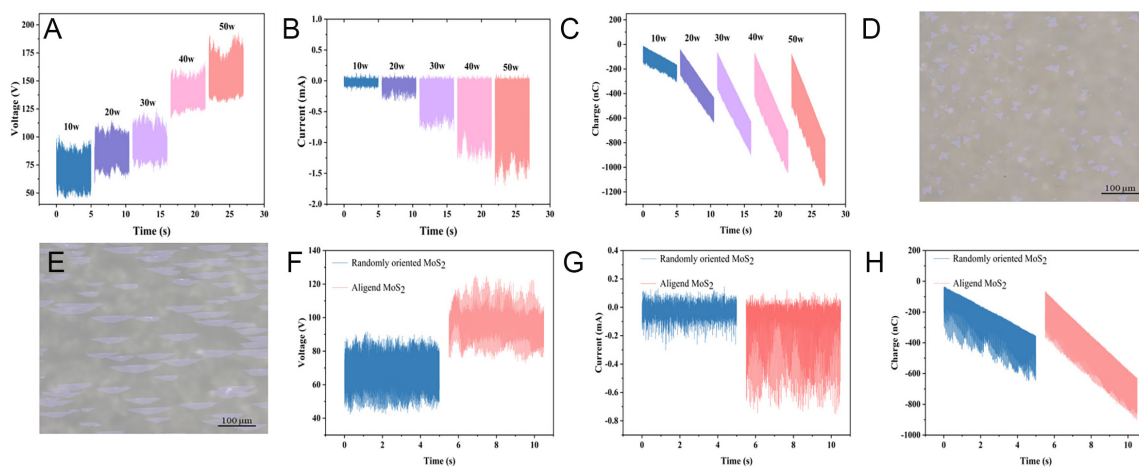
Figure 10. Aligned MoS$_2$-based TENG voltage (A), current (B), and charge (C) at different ultrasonic powers. Optical microscope image of randomly oriented MoS$_2$ (D) and aligned MoS$_2$ (E). Randomly oriented and aligned MoS$_2$-based TENG voltage (F), current (G), and charge (H).

MoS$_2$-PTFE electric double layer. In particular, the rise in charge accumulation within 5 s at both power levels (40-50 W) is not substantial due to the limitation of the device size on the total charge, and then the charge accumulation reaches its peak.

In order to investigate the electrical properties of randomly oriented MoS_2 and aligned MoS_2, we measure the device electrical signals by using two kinds of them as charge transport layers, respectively. The OM images of randomly oriented MoS_2 and aligned MoS_2 are shown in Figure 10D and E, respectively. As shown in Figure 10F-H, we select the voltage, current, and charge signals output from the device within 5 s for comparison while keeping other parameters consistent. The aligned MoS_2 device was able to output a voltage of 120 V, a peak current of 0.7 mA, and accumulate a charge of 900 nC under the same test conditions, whereas the randomly oriented MoS_2 device could only output a voltage of 85 V, a peak current of 0.2 mA, and an accumulated charge of 600 nC. The results of the superiority of aligned MoS_2 devices over randomly oriented MoS_2 devices can be demonstrated by the fact that grain boundaries and defects at the merging of randomly oriented MoS_2 grains lead to the compounding of a large number of electrons and holes during the charge transport process, which affects the transport of carriers. The MoS_2-based TENG generates high voltage, current, and accumulated charge under the influence of ultrasonic waves. Consequently, the aligned MoS_2 is regarded as a promising candidate for charge transfer.

CONCLUSIONS

In conclusion, a one-step deposition strategy was employed to prepare highly aligned MoS_2 nanosheets. Through the detailed characterization of MoS_2 nanosheets, it was observed that they have large dimensions and orientation rate of over 70%, which enables us to prepare aligned MoS_2 nanosheets at a low cost in a short period of time. Meanwhile, we employed a TENG as a charge transfer test probe to evaluate the charge transfer capability of aligned MoS_2 nanosheets under different ultrasonic powers. The aligned MoS_2 nanosheets exhibit high voltage, current, and charge under ultrasonic waves. The charge transport properties of randomly oriented and aligned MoS_2 were compared by TENG. Furthermore, compared with the conventional low-frequency mechanical work, choosing high-frequency ultrasound as the energy source broadens the scope application of aligned MoS_2 in the TENG field. This indicates that the aligned MoS_2 nanosheet exhibits considerable potential in charge transfer and energy harvesting applications.

DECLARATIONS

Author Contributions
Data curation, methodology, writing - original draft: Li, J.
Data curation, investigation: Guo, J.
Writing - review & editing: Zhang, Y.
Investigation: Zhang, A.
Formal analysis, project administration: Yang, W.
Formal analysis, resources: Feng, X.
Data curation, validation: Zhang, Y.
Funding acquisition, project administration: Yang, P.

Availability of data and materials
The detailed materials and methods in the experiment are available within the manuscript. Further data are available from the corresponding author upon reasonable request.

Foundation of the Chinese Academy of Sciences.

Conflicts of interest
All authors declared that there are no conflicts of interest.

Ethical approval and consent to participate
Not applicable.

Consent for publication
Not applicable.

Copyright

REFERENCES

1. Zhang, Z.; Yang, X.; Liu, K.; Wang, R. Epitaxy of 2D materials toward single crystals. *Adv. Sci.* **2022**, *9*, e2105201. DOI PubMed PMC
2. Yang, M.; Xiong, K.; Chen, X.; Zhong, H.; Lin, S. Ultra-low-power-consuming liquid-water-based optoelectronic computing chip. *Device* **2024**, *2*, 100547. DOI
3. Cheng, Z.; Cao, R.; Wei, K.; et al. 2D materials enabled next-generation integrated optoelectronics: from fabrication to applications. *Adv. Sci.* **2021**, *8*, e2003834. DOI PubMed PMC
4. Splendiani, A.; Sun, L.; Zhang, Y.; et al. Emerging photoluminescence in monolayer MoS_2. *Nano. Lett.* **2010**, *10*, 1271-5. DOI
5. Mak, K. F.; Lee, C.; Hone, J.; Shan, J.; Heinz, T. F. Atomically thin MoS_2: a new direct-gap semiconductor. *Phys. Rev. Lett.* **2010**, *105*, 136805. DOI PubMed
6. Zhang, X.; Nan, H.; Xiao, S.; et al. Shape-uniform, high-quality monolayered MoS_2 crystals for gate-tunable photoluminescence. *ACS. Appl. Mater. Interfaces.* **2017**, *9*, 42121-30. DOI
7. Liu, H.; Si, M.; Najmaei, S.; et al. Statistical study of deep submicron dual-gated field-effect transistors on monolayer chemical vapor deposition molybdenum disulfide films. *Nano. Lett.* **2013**, *13*, 2640-6. DOI
8. Kang, M.; Kim, S. J.; Song, W.; et al. Fabrication of flexible optoelectronic devices based on MoS_2/graphene hybrid patterns by a soft lithographic patterning method. *Carbon* **2017**, *116*, 167-73. DOI
9. Gautam, S.; Chugh, S.; Gates, B. D. Electrodeposition of PdPt nanoparticles on edges and S-vacancies in exfoliated MoS_2 nanosheets for enhanced hydrogen evolution activity. *ChemSusChem* **2024**, *17*, e202301922. DOI PubMed
10. Gao, Q.; Zhang, C.; Yang, K.; et al. High-performance CVD bilayer MoS_2 radio frequency transistors and gigahertz mixers for flexible nanoelectronics. *Micromachines* **2021**, *12*, 451. DOI PubMed PMC
11. Kim, J. K.; Song, Y.; Kim, T. Y.; et al. Analysis of noise generation and electric conduction at grain boundaries in CVD-grown MoS_2 field effect transistors. *Nanotechnology* **2017**, *28*, 47LT01. DOI
12. Khandelwal, G.; Deswal, S.; Shakthivel, D.; Dahiya, R. Recent developments in 2D materials for energy harvesting applications. *J. Phys. Energy.* **2023**, *5*, 032001. DOI
13. Priya, S.; Mandal, D.; Chowdhury, A.; Kansal, S.; Chandra, A. Time-dependent exfoliation study of MoS_2 for its use as a cathode material in high-performance hybrid supercapacitors. *Nanoscale. Adv.* **2023**, *5*, 1172-82. DOI PubMed PMC
14. Singh, A.; Mishra, A. K. Large area CVD-grown vertically and horizontally oriented MoS_2 nanostructures as SERS biosensors for single molecule detection. *Nanoscale* **2023**, *15*, 16480-92. DOI PubMed
15. Xu, C.; Pan, C.; Liu, Y.; Wang, Z. Hybrid cells for simultaneously harvesting multi-type energies for self-powered micro/nanosystems. *Nano. Energy.* **2012**, *1*, 259-72. DOI
16. Oh, H.; Kwak, S. S.; Kim, B.; et al. Highly conductive ferroelectric cellulose composite papers for efficient triboelectric nanogenerators. *Adv. Funct. Mater.* **2019**, *29*, 1904066. DOI
17. Ye, X.; Zheng, Z.; Werner, J. G.; Boley, J. W. Mechanically rupturing liquid metal oxide induces electrochemical energy (Adv. Funct. Mater. 31/2024). *Adv. Funct. Mater.* **2024**, *34*, 2470174. DOI
18. Yang, C.; He, J.; Guo, Y.; et al. Highly conductive liquid metal electrode based stretchable piezoelectric-enhanced triboelectric nanogenerator for harvesting irregular mechanical energy. *Mater. Des.* **2021**, *201*, 109508. DOI
19. Ahmadi, R.; Abnavi, A.; Hasani, A.; et al. Pseudocapacitance-induced synaptic plasticity of tribo-phototronic effect between ionic liquid and 2D MoS_2. *Small* **2024**, *20*, e2304988. DOI
20. Aji, A. S.; Nishi, R.; Ago, H.; Ohno, Y. High output voltage generation of over 5 V from liquid motion on single-layer MoS_2. *Nano. Energy.* **2020**, *68*, 104370. DOI
21. Kumar, S.; Sharma, A.; Gupta, V.; Tomar, M. Development of novel MoS_2 hydrovoltaic nanogenerators for electricity generation from moving NaCl droplet. *J. Alloys. Compd.* **2021**, *884*, 161058. DOI

22.   Wang, T.; Guo, J.; Zhang, Y.; et al. Synthesis of high-quality monolayer MoS_2 via a CVD upstream deposition strategy for charge capture and collection. *Cryst. Growth. Des.* **2024**, *24*, 2755-63. DOI

23.   van, Z. A. M.; Huang, P. Y.; Chenet, D. A.; et al. Grains and grain boundaries in highly crystalline monolayer molybdenum disulphide. *Nat. Mater.* **2013**, *12*, 554-61. DOI

24.   You, J.; Hossain, M. D.; Luo, Z. Synthesis of 2D transition metal dichalcogenides by chemical vapor deposition with controlled layer number and morphology. *Nano. Converg.* **2018**, *5*, 26. DOI PubMed PMC

25.   Zhao, T.; Guo, J.; Li, T.; et al. Substrate engineering for wafer-scale two-dimensional material growth: strategies, mechanisms, and perspectives. *Chem. Soc. Rev.* **2023**, *52*, 1650-71. DOI

26.   Chen, L.; Liu, B.; Ge, M.; Ma, Y.; Abbas, A. N.; Zhou, C. Step-edge-guided nucleation and growth of aligned WSe_2 on sapphire via a layer-over-layer growth mode. *ACS. Nano.* **2015**, *9*, 8368-75. DOI

27.   Yu, H.; Yang, Z.; Du, L.; et al. Precisely aligned monolayer MoS_2 epitaxially grown on h-BN basal plane. *Small* **2017**, *13*, 1603005. DOI

28.   Zhou, X.; Xue, X.; Cai, L.; Liu, S.; Liu, M.; Yu, G. Large-area orientation-controlled growth of hexagonal boron nitride on liquid copper. *ACS. Appl. Electron. Mater.* **2022**, *4*, 6261-8. DOI

29.   Aljarb, A.; Cao, Z.; Tang, H. L.; et al. Substrate lattice-guided seed formation controls the orientation of 2D transition-metal dichalcogenides. *ACS. Nano.* **2017**, *11*, 9215-22. DOI

30.   Ji, Q.; Kan, M.; Zhang, Y.; et al. Unravelling orientation distribution and merging behavior of monolayer MoS_2 domains on sapphire. *Nano. Lett.* **2015**, *15*, 198-205. DOI

31.   Park, Y.; Ahn, C.; Ahn, J. G.; et al. Critical role of surface termination of sapphire substrates in crystallographic epitaxial growth of MoS_2 using inorganic molecular precursors. *ACS. Nano.* **2023**, *17*, 1196-205. DOI

32.   Liu, L.; Li, T.; Ma, L.; et al. Uniform nucleation and epitaxy of bilayer molybdenum disulfide on sapphire. *Nature* **2022**, *605*, 69-75. DOI

33.   Li, T.; Guo, W.; Ma, L.; et al. Epitaxial growth of wafer-scale molybdenum disulfide semiconductor single crystals on sapphire. *Nat. Nanotechnol.* **2021**, *16*, 1201-7. DOI

34.   Wang, Q.; Li, N.; Tang, J.; et al. Wafer-scale highly oriented monolayer MoS_2 with large domain sizes. *Nano. Lett.* **2020**, *20*, 7193-9. DOI

35.   Ma, Z.; Wang, S.; Deng, Q.; et al. Epitaxial growth of rectangle shape MoS_2 with highly aligned orientation on twofold symmetry a-Plane sapphire. *Small* **2020**, *16*, e2000596. DOI

36.   Dong, J.; Liu, Y.; Ding, F. Mechanisms of the epitaxial growth of two-dimensional polycrystals. *NPJ. Comput. Mater.* **2022**, *8*, 797. DOI

37.   Ji, H. G.; Lin, Y.; Nagashio, K.; et al. Hydrogen-assisted epitaxial growth of monolayer tungsten disulfide and seamless grain stitching. *Chem. Mater.* **2018**, *30*, 403-11. DOI

38.   Yao, W.; Wu, B.; Liu, Y. Growth and grain boundaries in 2D materials. *ACS. Nano.* **2020**, *14*, 9320-46. DOI

39.   Yang, P.; Liu, F.; Li, X.; et al. Highly reproducible epitaxial growth of wafer-scale single-crystal monolayer MoS_2 on sapphire. *Small. Methods.* **2023**, *7*, e2300165. DOI

40.   Li, L.; Wang, Q.; Wu, F.; et al. Epitaxy of wafer-scale single-crystal MoS_2 monolayer via buffer layer control. *Nat. Commun.* **2024**, *15*, 1825. DOI PubMed PMC

41.   Rajan A, Warner JH, Blankschtein D, Strano MS. Generalized mechanistic model for the chemical vapor deposition of 2D transition metal dichalcogenide monolayers. *ACS. Nano.* **2016**, *10*, 4330-44. DOI PubMed

42.   Kang, L.; Tian, D.; Meng, L.; et al. Epitaxial growth of highly-aligned MoS_2 on c-plane sapphire. *Surf. Sci.* **2022**, *720*, 122046. DOI

43.   Su, L.; Zhang, Y.; Yu, Y.; Cao, L. Dependence of coupling of quasi 2-D MoS_2 with substrates on substrate types, probed by temperature dependent Raman scattering. *Nanoscale* **2014**, *6*, 4920-7. DOI

44.   Ling, X.; Lee, Y. H.; Lin, Y.; et al. Role of the seeding promoter in MoS_2 growth by chemical vapor deposition. *Nano. Lett.* **2014**, *14*, 464-72. DOI

45.   Najmaei, S.; Liu, Z.; Zhou, W.; et al. Vapour phase growth and grain boundary structure of molybdenum disulphide atomic layers. *Nat. Mater.* **2013**, *12*, 754-9. DOI

46.   Li, J.; Wang, S.; Jiang, Q.; et al. Single-crystal MoS_2 monolayer wafer grown on Au (111) film substrates. *Small* **2021**, *17*, e2100743. DOI

47.   Wu, S.; Zeng, Y.; Zeng, X.; et al. High-performance p-type MoS_2 field-effect transistor by toroidal-magnetic-field controlled oxygen plasma doping. *2D. Mater.* **2019**, *6*, 025007. DOI

48.   Xu, X.; Pan, Y.; Zhong, Y.; Ge, L.; Jiang, S. P.; Shao, Z. From scheelite $BaMoO_4$ to perovskite $BaMoO_3$: enhanced electrocatalysis toward the hydrogen evolution in alkaline media. *Compos. Part. B. Eng.* **2020**, *198*, 108214. DOI